https://doi.org/10.5194/wcd-2020-41
Preprint. Discussion started: 3 September 2020
© Author(s) 2020. CC BY 4.0 License.

Weather and Climate Dynamics Discussions
Open Access
EGU

Polar Lows – Moist Baroclinic Cyclones Developing in Four Different Vertical Wind Shear Environments

Patrick Johannes Stoll[1], Thomas Spengler[2], Annick Terpstra[2], and Rune Grand Graversen[1,3]

[1]Department of Physics and Technology, Arctic University of Norway, Tromsø, Norway
[2]Geophysical Institute, University of Bergen, and Bjerknes Centre for Climate Research, Bergen, Norway
[3]Norwegian Meteorological Institute, Norway

Correspondence: Patrick Johannes Stoll (patrick.stoll@uit.no)

Abstract. Polar lows are intense mesoscale cyclones that develop in polar marine air masses. Motivated by the large variety in their proposed intensification mechanisms, cloud structure, and ambient sub-synoptic environment, we use self-organising maps to classify polar lows. The method is applied to 370 polar lows in the North-East Atlantic, which were obtained by matching mesoscale cyclones from the ERA-5 reanalysis to polar lows registered by the Norwegian Meteorological Institute in the STARS dataset. ERA-5 reproduces 93% of the STARS polar lows.

We identify five different polar-low configurations, which are characterised by the vertical wind shear vector relative to the propagation direction. Four categories feature a strong shear with different orientations of the shear vector, whereas the fifth category contains conditions with weak shear. The orientation of the vertical-shear vector for the strong shear categories determines the dynamics of the systems, confirming the relevance of the previously identified categorisation into forward and reverse-shear polar lows. In addition, we expand the categorisation with right and left-shear polar lows that propagate towards colder and warmer environments, respectively.

Polar lows in the four strong shear categories feature an up-shear tilt in the vertical, typical for the intensification through moist baroclinic processes. As weak-shear conditions mainly occur at the mature or lysis stage of polar lows, we find no evidence for hurricane-like development and propose that spirali-form PLs are most likely associated with a warm seclusion process.

1 Introduction

Polar lows (PLs) are intense mesoscale cyclones with a typical diameter of 200 - 500 km and a short lifetime of 6 - 36 h that develop in marine cold-air outbreaks during the extended winter season (e.g Rasmussen and Turner, 2003; Yanase et al., 2004; Claud et al., 2004; Renfrew, 2015; Rojo et al., 2015). Despite numerical-weather prediction (NWP) models being capable to simulate these systems, operational forecasts still have have issues predicting the exact location and intensity of PLs (e.g. Kristjánsson et al., 2011; Føre et al., 2012; Stoll et al., 2020). Several paradigms have been proposed to describe PL development, ranging from baroclinic instability (e.g. Harrold and Browning, 1969; Reed, 1979; Reed and Duncan, 1987) to symmetric hurricane-like growth (e.g. Rasmussen, 1979; Emanuel and Rotunno, 1989). The multitude of paradigms demonstrates that our dynamical interpretation of these systems is still lacking (Jonassen et al., 2020). To further alleviate this shortcoming,

https://doi.org/10.5194/wcd-2020-41
Preprint. Discussion started: 3 September 2020
© Author(s) 2020. CC BY 4.0 License.

we present a classification of PLs by their structure and sub-synoptic environment to identify the relevance of the proposed paradigms.

The proposed PL paradigms often stem from the different cloud structures (Forbes and Lottes, 1985; Rojo et al., 2015) and sub-synoptic environments (Duncan, 1978; Terpstra et al., 2016). From the 1980s, the PL spectrum was thought to range from pure baroclinic PLs with a comma-shaped cloud structure to convective systems with a spirali-form cloud signature like hurricanes (p.157 Rasmussen and Turner, 2003). The latter usually invoked either conditional instability of the second kind (CISK Charney and Eliassen, 1964; Ooyama, 1964) or wind induced surface heat exchange (WISHE Emanuel, 1986) as mechanisms for intensification. However, most PLs appear as hybrids between the ends of this spectrum (Bracegirdle and Gray, 2008).

Using idealised simulations to map the sensitivities of cyclone development in this spectrum, Yanase and Niino (2007) found that cyclones intensify fastest in an environment with high baroclincity, where latent heat release supports the development. Thus, PLs are mostly characterised by moist baroclinic instability and neither dry baroclinic nor pure CISK modes grow fast enough to explain their development (Sardie and Warner, 1983; Terpstra et al., 2015).

Furthermore, hurricane-like PLs do usually not resemble the structure of hurricanes and instead feature asymmetric updrafts typical of baroclinic development with latent heating not playing the dominant role (Føre et al., 2012; Kolstad et al., 2016; Kolstad and Bracegirdle, 2017). The PLs that appear hurricane-like in their mature stage were also observed to be initiated by baroclinic instability (e.g. Nordeng and Rasmussen, 1992; Føre et al., 2012).

Several categorisations of PLs were proposed to shed light on the development pathways of PLs (e.g. Duncan, 1978; Businger and Reed, 1989; Rasmussen and Turner, 2003; Bracegirdle and Gray, 2008; Terpstra et al., 2016). Duncan (1978) suggested a categorisation based on the vertical wind shear angle of the PL environment, defined as the angle between the tropospheric mean wind vector and the thermal wind vector. Situations where the vectors point in the same (opposite) direction are referred to as forward (reverse) shear conditions. PLs have been found to occur in both forward-shear (e.g. Reed and Blier, 1986; Hewson et al., 2000) and reverse-shear environments (e.g. Reed, 1979; Bond and Shapiro, 1991; Nordeng and Rasmussen, 1992), where both types of PLs occur approximately equally often (Terpstra et al., 2016).

PLs in forward-shear environments develop similar to typical mid-latitude cyclones in a deep-baroclinic zone with an associated upper-level jet. They have the cold air to the left with respect to their direction of propagation and are mainly propagating eastward (Terpstra et al., 2016). PLs in reverse-shear environments, on the other hand, often develop in the vicinity of an occluded low pressure system and are characterised by a low-level jet. They have the cold air to the right with respect to their propagation direction and are mainly propagating southward. Reverse-shear PLs also feature considerably higher surface heat fluxes and a lower static stability in the troposphere, expressed by a larger temperature contrast between the temperature at the sea surface and at 500 hPa (Terpstra et al., 2016).

However, assigning PL environments solely based on two types of shear might be insufficient to characterise PLs. Furthermore, the shear angle cannot distinguish between baroclinically- and convectively-driven systems, hence it cannot address the hurricane-like part of the PL spectrum. To alleviate this shortcoming, we categorise PLs based on their sub-synoptic environment using self-organising maps (SOM, see Section 2.5) without an *a-priori* determination of a variable used for the categori-

https://doi.org/10.5194/wcd-2020-41
Preprint. Discussion started: 3 September 2020
© Author(s) 2020. CC BY 4.0 License.

sation. The thereby identified meteorological configurations reveal the underlying PL intensification mechanisms, allowing us to investigate the following research questions:

- What are the archetypal meteorological conditions during PL development?
- Can the existing PL classification be confirmed or should it be revised?
- What are the pertinent intensification mechanisms?

2 Methods

2.1 Polar-low list

This study is based on a modified version of the STARS (Sea Surface Temperature and Altimeter Synergy for Improved Forecasting of Polar Lows) dataset (Rojo et al., 2019, henceforth Rojo list). This list includes the location and time of PLs detected from AVHRR satellite images over the North-East Atlantic that were listed in the STARS dataset by the Norwegian Meteorological Institute between November 1999 and March 2019 (Noer and Lien, 2010). The STARS dataset has been used for several previous PL studies (e.g. Laffineur et al., 2014; Zappa et al., 2014; Rojo et al., 2015; Terpstra et al., 2016; Smirnova and Golubkin, 2017; Stoll et al., 2018).

The advantage of the Rojo list compared to the STARS dataset is that it contains considerably more PLs. While the STARS dataset only contains the major PL in situations of multiple PL developments, the Rojo list includes the location of all individual PLs (Rojo et al., 2015). Thus, the Rojo list includes 420 PLs, which are associated with the 262 PL events in the STARS database of which 183 PL events feature a single PL and the remaining 79 events have 2 - 4 PLs per event. In addition, the Rojo list classifies the cloud morphology for each detected PL time step.

As the Rojo list includes individual time steps of each PL when AVHRR satellite images were available, the time interval between observations is irregular and ranges between 30 minutes and up to 12 hours. This also implies that the list lacks the genesis and lysis time of some PLs.

2.2 Polar-low tracks in ERA-5

We use fields from the European Centre for Medium-Range Weather Forecasts (ECMWF) state-of-the-art reanalysis version 5 (ERA-5 Hersbach and Dee, 2016) to track PLs and analyse the atmospheric environment. The ability of ERA-5 to simulate PLs has not yet been investigated, though some studies have shown that atmospheric models with a comparable horizontal resolution to ERA-5 are capable to produce most PL cases (Smirnova and Golubkin, 2017; Stoll et al., 2018). As other studies estimated the amount of represented STARS PLs in ERA-Interim to 48% Smirnova and Golubkin (2017), 55% (Zappa et al., 2014), 60% (Michel et al., 2018), and 69% (Stoll et al., 2018), we anticipate the performance of ERA5 to be even higher.

ERA-5 provides data from 1950 to the near-present at hourly resolution with a spectral truncation of T639 in the horizontal, which is equivalent to a grid spacing of about 30 km. The data has 137 hybrid levels in the vertical, of which approximately 47

https://doi.org/10.5194/wcd-2020-41
Preprint. Discussion started: 3 September 2020
© Author(s) 2020. CC BY 4.0 License.

are below 400 hPa, which is the typical height of the tropopause at high latitudes. We obtained the data at a lat × lon grid of 0.25° × 0.5° within 50° - 85°N and 40°W - 65°E. We chose a coarser grid spacing for the longitudes due to their convergence towards the pole. We use data from the surface and from the pressure levels at 925, 850, 700 and 500 hPa.

To analyse the PL development, we derive PL tracks with an hourly resolution by applying the mesoscale tracking algorithm developed by Watanabe et al. (2016) and retain the tracks that match the Rojo list. The tracking procedure is based on detecting local maxima in relative vorticity at 850 hPa, where we tuned the parameters in the tracking algorithm with the objective to obtain a good match with the Rojo list.

In particular, we modified the algorithm as follows:

- No land mask is applied to account for PLs propagating partially over land.
- A uniform filter with a 60 km radius is applied to the relative vorticity to reduce artificial splitting of PL tracks and to smooth the tracks.
- The threshold for the vortex peak $\zeta_{max,0}$ is $1.5 \cdot 10^{-4}\,\mathrm{s}^{-1}$, and the threshold for the vortex area $\zeta_{min,0}$ is $1.2 \cdot 10^{-4}\,\mathrm{s}^{-1}$.
- We do not require a filter for synoptic-scale disturbances, as the matching to the Rojo list ensures that the tracks include PLs only.

All tracks that have a distance of less than 150 km to a PL from the Rojo list for at least one time step are regarded as matches. Hereby, 374 of the 420 PL centres from the Rojo list have at least one associated PL track. In total, however, we obtain 556 associated PL tracks, where multiple matches to the same PL from the Rojo list have two reasons. Firstly, ERA-5 features multiple PLs connected to the PL centre from the Rojo list. Secondly, the tracking algorithm yields several track segments for the same PL. The latter occurs if the location of the vorticity maximum moves within an area of high vorticity, e.g., a frontal zone. In these cases, two track segments are merged if the time gap between them is less than 6 hours and if the extrapolation of one track segment over the time gap includes the other segment within a distance of 150 km. This merging was applied for 86 PL tracks.

We exclude tracks if the lifetime is shorter than 5 hours (54 tracks) and if the track is over land for most of the PL lifetime (5 tracks). The latter is defined as the initial, middle, and final time step of the PL occurring on land. Other land exclusion methods were tested and gave similar results. If a track is included twice, which occurs when it matches with two PLs from the Rojo list, one is removed (37 tracks).

Applying this procedure, a total of 374 of the total 556 PL tracks is retained with 13,221 hourly time steps. These 374 PLs are associated with 243 PL events from the Rojo list. Hence, 243 of the 262 PL events (93%) from the Rojo list are matched to cyclones in ERA-5 and the number of detected PL tracks (374) is close to the number of PLs included the Rojo list (420). This highlights the capability of ERA-5 to represent most PL events and that the applied tracking and matching procedure is successful. Furthermore, our detection rate indicates that ERA-5 is superior to its predecessor ERA-Interim when it comes to capturing PLs, where Stoll et al. (2018) detected 55% and Michel et al. (2018) about 60% of the STARS PLs in ERA-Interim.

https://doi.org/10.5194/wcd-2020-41
Preprint. Discussion started: 3 September 2020
© Author(s) 2020. CC BY 4.0 License.

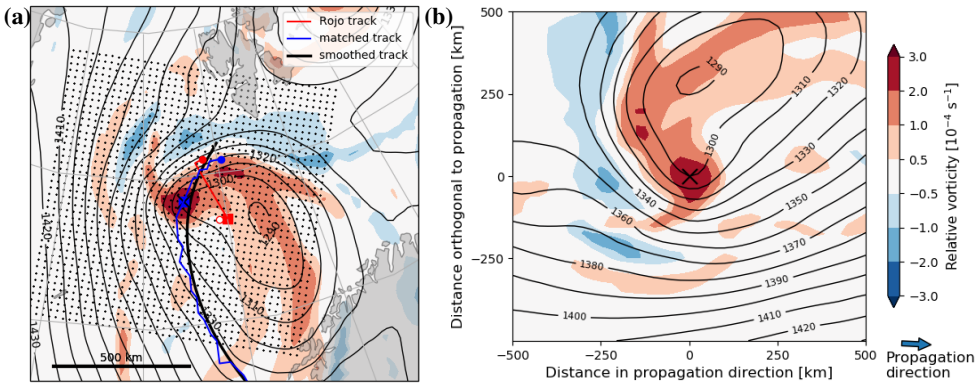

Figure 1. Exemplary depiction of deriving the PL-centred analysis. (a) Relative vorticity at 850 hPa (shading) and geopotential height at 850 hPa (contours, spacing 10 m) for 20 March 2001 01:00 UTC. The track of polar low number 10 from the Rojo list is shown in red and the matched track is depicted in blue. The location at the selected time are indicated by squares. The smoothed track is depicted in black, the propagation direction of the PL at the selected time is southward. The location of the grid cells of the polar-low centred analysis domain are denoted by black dots. (b) Same fields as for (a) in the polar-low centred domain, constructed such that the polar-low centre is in the middle (black 'x') and the propagation direction is towards the right.

Note that the match rates strongly depends on the applied matching criteria. The matching criteria applied here is stronger than the one applied in Stoll et al. (2018).

2.3 Polar-low centred analysis

We employ a PL-centred analysis, where meteorological fields from ERA-5 for each individual time step of a PL track are transformed onto a PL-centred grid. The cells of the PL-centred grid (black dots in Figure 1) are derived from the location and propagation direction of the PL. The propagation direction is obtained by applying a cubic-spline smoothing to the PL track points (De Boor et al., 1978). We smooth, because the tracks can feature non-monotonous behaviour due to the discrete nature of the grid and varying locations of the vorticity maxima in areas of enhanced vorticity, such as frontal zones. Smoothing also provides continuous tracks in situations of low propagation speed, where the propagation direction is highly variable

All meteorological fields from ERA-5 were linearly interpolated onto the PL-centred grid with an extent of 1000×1000 km with a grid spacing of 25 km (see Fig. 1). Given a typical PL diameter between 150 and 600 km (Rojo et al., 2015), this grid covers the PL and its sub-synoptic environment.

We exclude time steps where this grid is not fully within the chosen ERA-5 boundaries (Section 2.2). This reduces the PL time steps from 13,221 to 12,695 and removes 4 of the 374 PLs for their complete lifetime. As most of the excluded time steps occur at the end of the PL lifetime, this exclusion has only a small influence on our analysis of the PL intensification.

https://doi.org/10.5194/wcd-2020-41
Preprint. Discussion started: 3 September 2020
© Author(s) 2020. CC BY 4.0 License.

2.4 Parameter preparation

In addition to standard meteorological variables, we derived an additional set of parameters using grid points within a radius of 250 km around the PL centre. For near-surface parameters, such as the 10 m wind vector, the turbulent heat fluxes, and parameters partly derived from low-levels, such as the Brunt-Väisälä frequency, only grid cells over open ocean, defined by a water fraction larger than 80%, are included.

We estimate the tropospheric **Brunt-Väisälä frequency**, N, using the potential temperature, θ, at 500 and 925 hPa

$$N = \sqrt{\frac{g}{\overline{\theta}}\frac{\partial\theta}{\partial z}} \approx \sqrt{\frac{g}{(\theta_{500}+\theta_{925})/2}\frac{\theta_{500}-\theta_{925}}{z_{500}-z_{925}}} \tag{1}$$

with gravitational constant $g = 9.8\,\mathrm{ms}^{-2}$ and geopotential height z. Afterwards, we apply a radial average.

The **differential wind vector** is computed using the mean wind vectors at 500 and 925 hPa,

$$\Delta\overline{\boldsymbol{u}} = (\Delta\overline{u}, \Delta\overline{v}) = (\overline{u_{500}} - \overline{u_{925}}, \overline{v_{500}} - \overline{v_{925}}), \tag{2}$$

where an overbar indicates the mean computed within a radius of 500 km around the PL centre. The upper-level (500 hPa) is considerably higher than the level chosen by Terpstra et al. (2016) (700 hPa). Given that PLs span the entire depth of the polar troposphere, we chose one level from the lower and one from the upper troposphere, with neither level intersecting with the sea surface or the tropopause.

We define the **vertical-shear strength** as

$$\left|\frac{\Delta\overline{\boldsymbol{u}}}{\Delta\overline{z}}\right| = \frac{|\Delta\overline{\boldsymbol{u}}|}{\overline{z_{500}} - \overline{z_{925}}}. \tag{3}$$

The **vertical-shear angle**, $\alpha = [\alpha_s - \alpha_p]\,(\mathrm{mod}\ 360°)$, is derived from the angle between the differential wind vector, $\Delta\overline{\boldsymbol{u}}$, and the propagation direction, α_p, of the PL. The propagation vector of the PL appears to be a good estimate of the mean wind encountered by the PL (Fig. 3). Different to Terpstra et al. (2016), we compute the radial average before calculating the angle. Thereby, our method obtains the shear angle of the environmental mean flow and partially filters for perturbations induced by the PL itself. Also to reduce the influence of the PL-induced perturbations, a large radius of 500 km is applied for the computation of the differential wind vector. Note, that the shear angle by this computation takes values between 0 and 360° and not between 0 and 180° as in Terpstra et al. (2016). In addition, we define the **vertical-shear vector** in the propagation direction

$$\left(\frac{\Delta\overline{\boldsymbol{u}}}{\Delta\overline{z}}\right)_p = \left|\frac{\Delta\overline{\boldsymbol{u}}}{\Delta\overline{z}}\right| \cdot (\cos(\alpha), \sin(\alpha)). \tag{4}$$

Our method is different to Duncan (1978) and Terpstra et al. (2016), though tests confirm that their thermal wind vector is similar to the vertical-shear vector utilised in this study.

The **vorticity tendency** of the PL time steps is obtained from the first derivative in time of the vorticity maxima that was used for the detection of the PL. These maxima are based on the spatially-smoothed vorticity using a uniform filter of 60 km radius.

https://doi.org/10.5194/wcd-2020-41
Preprint. Discussion started: 3 September 2020
© Author(s) 2020. CC BY 4.0 License.

However, the time evolution in the vorticity is still discontinuous (see Supplementary figure 1). Therefore a Savitzky-Golay filter (Savitzky and Golay, 1964) is applied on the time evolution in the vorticity for the computation of the first derivative. This filter applies a least-square regression in our case of a second-order polynomial within a window of eleven vorticity time steps, or the whole lifetime if it is shorter than ten hours. The **growth rate** is computed by the fraction of the vorticity tendency to the vorticity of an time step.

2.5 Self-organising maps (SOM)

Kohonen et al. (2001) developed the SOM method for displaying typical patterns in high-dimensional data. The patterns, also referred to as nodes, are ordered in a 2-D array with neighbouring nodes being more similar to each other than nodes with a longer distance in the array. Kohonen et al. (2001) originally developed the method for artificial neural networks, but it has been extensively applied in many fields of science in the last years, including climate data analysis (e.g. Nygård et al., 2019).

We apply the package described in Wehrens et al. (2007) for the computation. The size of the node array has to be subjectively determined for the dataset at hand and is typically determined after some testing. We find an array of 3×3 nodes to be most suitable, reducing 12,695 PL-centred fields to 3×3 archetypal nodes. Larger arrays mainly display additional details of minor interest (Supplementary Figure 2), whereas smaller arrays merge nodes that contained relevant individual information.

We chose the temperature anomaly field at 850 hPa of each time step $T'(x,y) = T(x,y) - \overline{T}(x,y)$ as a basis for the SOM analysis. In this way, the information if a PL occurred in a relatively warm or cold environment is removed, which would otherwise dominate the SOM analysis (Supplementary Figure 3 and 4). Thereby, the intrinsic temperature structure is most apparent. We also applied the SOM algorithm to several other atmospheric fields, which are presented and discussed in the supplementary material section 3. The SOM matrices produce similar patterns of variability when applied to the temperature anomaly field at other levels, the specific humidity anomaly, and the upper and lower-level geopotential height anomaly (see supplementary material). This demonstrates the generality of the results obtained from the temperature anomaly field at 850 hPa.

An advantage of the orientation of the PL-centred fields by the propagation direction is a reduction of the variability in the mid-level flow, as the mid-level flow largely determines the propagation of the PLs. Therefore, the SOM matrix obtained using the mid-level geopotential height anomaly produce nodes that are quite similar to each other (see Supplementary Figure 7). This expresses a small variability among PLs based on this variable and that PLs are generally characterised by a mid-level trough within a background flow in the propagation direction of the PL.

The time steps within each node can be associated with different PL phases, such as genesis, maturity, and lysis. The mature stage of the PL is here defined as the time step with the maximum spatially-filtered relative vorticity at 850 hPa, as utilised in the tracking algorithm (see Supplementary Figure 1). A PL can transition through several SOM nodes during its lifetime, which can be tracked through the SOM matrix. Evolution primarily occurs between neighbouring SOM nodes, as neighbours in the SOM matrix are most similar. Sometimes PLs transition back and forth between nodes, which means that the system is in a state between two nodes. We remove this back and forth development as it does not express a clear transition of the system.

https://doi.org/10.5194/wcd-2020-41
Preprint. Discussion started: 3 September 2020
© Author(s) 2020. CC BY 4.0 License.

3 Typical polar-low configurations

3.1 Patterns of variability

The SOM nodes have horizontal temperature anomaly fields resembling different strength and orientation of the temperature gradient with respect to the propagation direction of the PLs (Fig. 2). Nodes in the corners are the most extreme by construction of the SOM algorithm and therefore include the strongest horizontal temperature gradients. Nodes on opposing sides of the matrix display temperature anomaly fields that are most different from each other.

PLs in SOM node 1 and 9 propagate approximately perpendicular to the horizontal temperature gradient at 850 hPa with the cold side to the left and right, respectively. Thus, nodes 1 and 9 represent the classical forward and reverse-shear conditions, respectively (e.g. Forbes and Lottes, 1985; Terpstra et al., 2016). The other two nodes in the corner of the SOM matrix, node 3 and 7, also feature a large horizontal temperature gradient. PLs in node 3 are propagating towards lower temperatures. The opposite is evident in node 7 with PLs propagating towards higher temperatures. The remaining nodes display intermediate states with weaker temperature gradients, where none of the nodes resemble axis-symmetric characteristics that would be typical for hurricane-like PLs.

The nodes have characteristic upper (500 hPa) and lower-level (1000 hPa) flow fields (Fig. 2), where PLs in node 1 have a closed low-level circulation and an upper-level trough located up-shear. PLs in node 3 feature a weaker low-level circulation and a weak upper-level trough positioned slightly up-shear. Node 7 feature a short-wave low-level trough with an axis tilted from the PL centre to the left and downstream of the propagation direction, whereas the upper levels feature a trough located up-shear with an axis to the left and upstream of the direction of propagation. PLs in node 9 have a closed and weak upper-level circulation and a low-level trough slightly up-shear of the upper-level circulation with an axis oriented to the left of the direction of propagation.

The medium-level cloud cover associated with each node has a distinct distribution and location of its maximum (Fig. 2), which coincides with the region where the main updrafts occur (not shown). All nodes have a comma-shaped medium-level cloud cover with a different orientation, typically along the warm front on the cold side of the PL centre.

PLs transition between SOM nodes during their life cycle (Fig. 2), which means that the orientation of the environmental flow as compared to the thermal field can change for an individual PL. Also the strength of the environmental temperature gradient varies. At genesis times (green circles in Fig. 2), PLs are most frequently associated with the SOM nodes in the corners (Fig. 2). These situations feature a strong horizontal temperature gradient. Genesis occurs most often in forward (node 1+2: 26%) and reverse shear (node 9: 24%), though also right (node 3: 11%) and left shear (node 7: 14%) are common genesis situations. The SOM nodes associated with a low horizontal temperature contrast (5, 6 and 8) are predominantly lysis situations. Hence, PLs often evolve from nodes with stronger to nodes with weaker temperature gradients in the SOM matrix.

3.2 Connection to vertical wind shear

In the forward-shear nodes 1 and 2, the cold air is to the left of the propagation direction of the PL (Fig. 2), which is associated with a vertical-shear vector in the direction of propagation (Fig. 4) and thus an intensification of the area-mean wind vector

https://doi.org/10.5194/wcd-2020-41
Preprint. Discussion started: 3 September 2020
© Author(s) 2020. CC BY 4.0 License.

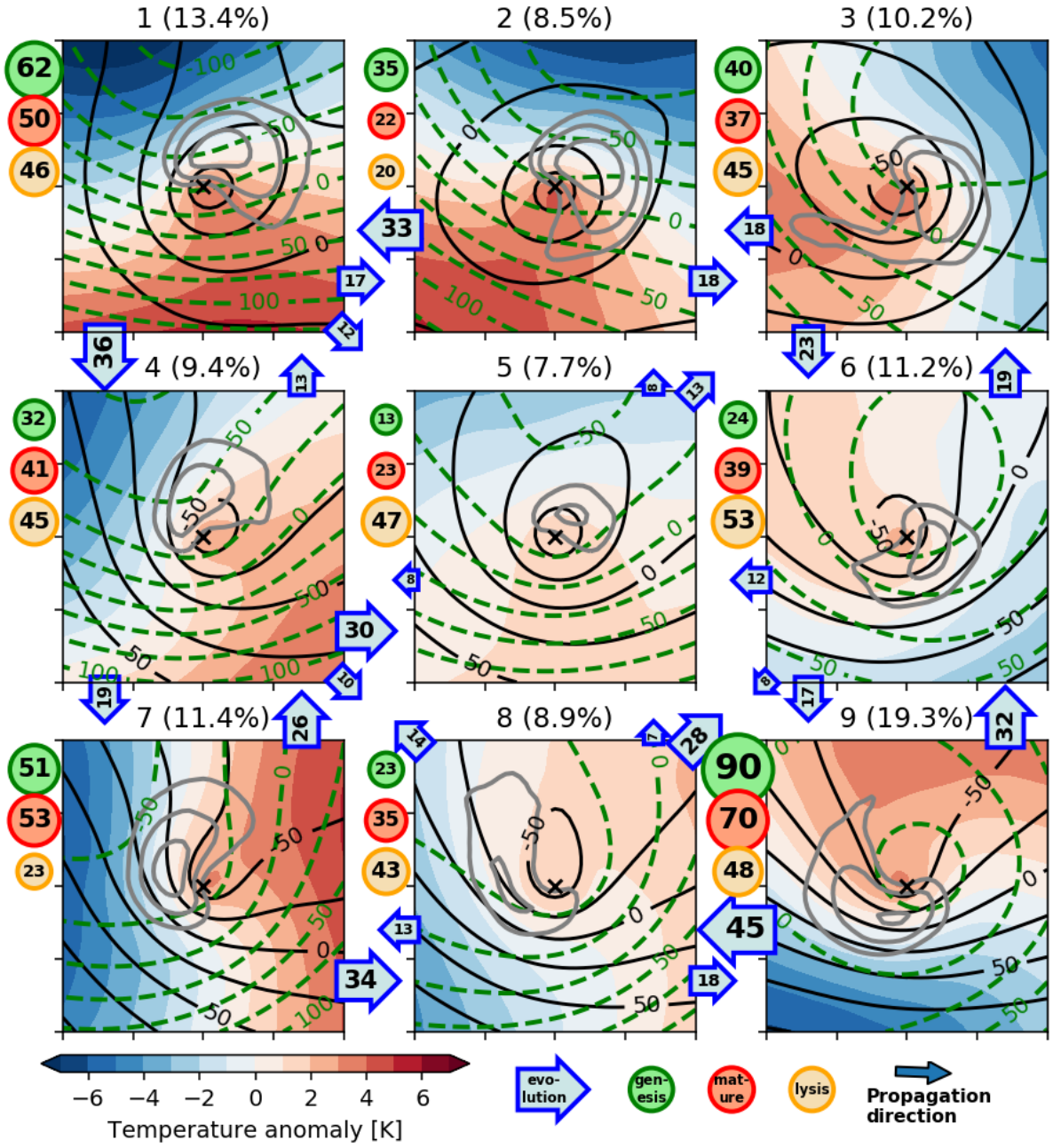

Figure 2. The self-organising map based on the 850 hPa temperature anomaly (T') using 12,695 PL time steps in a PL-centred grid as derived in Figure 1. The black 'x' marks the PL centre, ticks on x and y-axis are spaced at 250 km. Displayed is the composite of the 850 hPa temperature anomaly (shading), 1000 hPa geopotential height anomaly (black contours, spacing 25 m), 500 hPa geopotential height anomaly (green dashed contours, spacing 25 m) and medium-level cloud-cover fraction (grey contours at 0.7, 0.8 and 0.9). The number labels the SOM nodes and the percentage of time steps represented by the respective node. Green, red, and yellow circles indicate the number of genesis, mature, and lysis stages within each node. The numbers in the arrows indicate the amount of transitions between two nodes, where numbers smaller than 5 are not displayed.

https://doi.org/10.5194/wcd-2020-41
Preprint. Discussion started: 3 September 2020
© Author(s) 2020. CC BY 4.0 License.

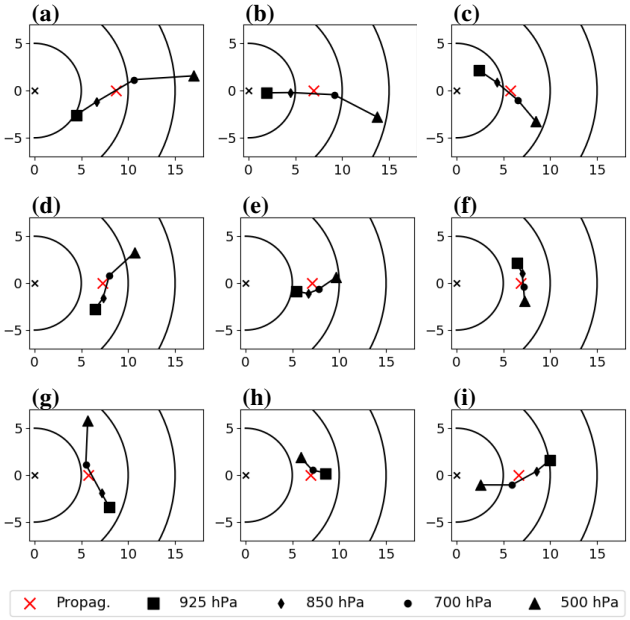

Figure 3. The mean hodographs associated with each SOM node displayed with the propagation direction towards the right. The square, diamond, circle, and triangle mark the SOM-mean, area-mean wind vector of the 925, 850, 700 and 500 hPa, respectively. The mean wind vectors are rotated with respect to the propagation vector of the polar low (red cross). Units on the x and y-axis are ms^{-1}. The origin is marked by a black "x" and black circular lines denote mean wind vectors with a strength of 5, 10 and 15ms^{-1}.

with height (Fig. 3a). The area-mean wind vector has a strength of more than 16 ms^{-1} at 500 hPa, but decreases to less than 5 ms^{-1} at 925 hPa (Fig. 3). Weak area-mean wind vectors indicate that the wind vectors cancel each other due to the closed cyclonic circulation near the surface (Fig. 2).

The reverse shear node 9 is the opposite to node 1 and 2 and features cold air to the right of the direction of propagation and thus a vertical-shear vector oriented opposite to the direction of propagation (Fig. 4). Reverse shear corresponds to a decrease of the strength of the mean wind vector with height, from 10 ms^{-1} at 925 hPa to 3 ms^{-1} at 500 hPa (Fig. 3). This is consistent with Bond and Shapiro (1991) and Terpstra et al. (2016), who observed that reverse-shear systems are often accompanied by a strong low-level jet. Accordingly, reverse-shear conditions are characterised by an almost closed upper-level circulation and a strong near-surface trough (see Fig. 2).

The other two nodes with a strong vertical shear, node 3 and 7, have intermediate shear angles between forward and reverse conditions. PLs in node 3 are propagating towards colder air masses (Fig.2). The environmental flow of node 3 features warm-air advection associated with veering, a clockwise turning of the wind vector with height (Fig. 3c). The vertical wind shear is towards the right of the direction of propagation with an angle of 50±20° and hence node 3 is referred to as right-shear conditions.

https://doi.org/10.5194/wcd-2020-41
Preprint. Discussion started: 3 September 2020
© Author(s) 2020. CC BY 4.0 License.

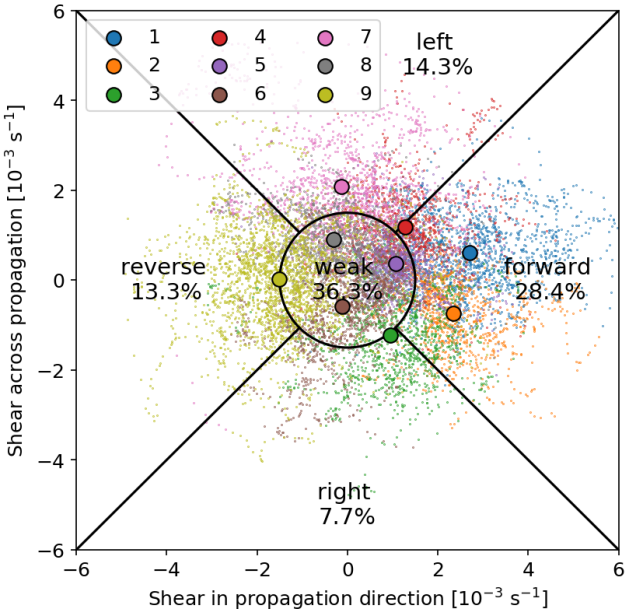

Figure 4. The categorisation along the vertical-shear vector (Equation 4). The shear vector of each polar-low time step is displayed as a small dot in the colour that represents the SOM node of the time step. The mean value of the shear vector of all time steps associated with each node is marked by a thick dot. The black circle and lines divide the shear-vector space into the categories forward shear, right shear, reverse shear, left shear and weak shear situations. The fraction of time steps associated with each category is displayed.

Node 7 is opposite to node 3, with PLs propagating towards warmer air masses featuring environmental cold-air advection associated with backing, an anti-clockwise rotation of the wind vector with height (Fig. 3g). The vertical wind shear is towards the left of the propagation direction at an angle of -90±30°. Hence, node 7 is referred to as left-shear condition, where the geostrophic flow features an upper-level trough with its axis tilted perpendicular to the left of the low-level trough axis. The same is the case for node 3, but the axis are perpendicular in the opposite direction.

Node 4 represents an intermediate setup between node 1 and 7 with intermediate values in the shear angle (Fig. 4 -45± 20°). In the remaining nodes (5, 6 and 8) the vertical-shear strength is weak and hence the angle of the vertical shear is of less importance. The mean wind vectors of these nodes at different heights are almost uniform (Fig. 3) indicating that the flow is quasi-barotropically aligned (Fig. 2).

Given that the vertical-shear vector with respect to the propagation direction captures the different SOM nodes (Fig. 4) we suggest to use it as the key parameter to classify PLs as defined in Table 1. Sorting all PLs by their shear in propagation and cross-propagation direction, a continuous spectrum emerges (Fig. 4). While this implies that strict thresholds are to some degree arbitrary, the choice of the exact thresholds was found to have no qualitative influence on the following results.

Applying a straight forward sectioning of the parameter space (Fig 4), forward-shear situations generally occur more often (28.4%) than reverse-shear situations (13.3%). Left-shear conditions (14.3%) are approximately as frequent as reverse shear

https://doi.org/10.5194/wcd-2020-41
Preprint. Discussion started: 3 September 2020
© Author(s) 2020. CC BY 4.0 License.

Table 1. Definition of the vertical-shear categories as depicted in Figure 4.

Category	shear angle	shear strength
Forward	-45° to 45°	$> 1.5 \cdot 10^{-3}\ \mathrm{s}^{-1}$
Right	45° to 135°	$> 1.5 \cdot 10^{-3}\ \mathrm{s}^{-1}$
Reverse	135° to -135°	$> 1.5 \cdot 10^{-3}\ \mathrm{s}^{-1}$
Left	-135° to -45°	$> 1.5 \cdot 10^{-3}\ \mathrm{s}^{-1}$
Weak	all	$\leq 1.5 \cdot 10^{-3}\ \mathrm{s}^{-1}$

conditions and right-shear situations are rather seldom (7.7%). In the following, these four categories are labelled as strong shear categories. In contrast, approximately 36.3% of the time steps have a weak shear of less than $1.5 \cdot 10^{-3}\,\mathrm{s}^{-1}$, which means that the wind vector is changing less than $1.5\,\mathrm{ms}^{-1}$ per km altitude.

3.3 Characteristics of the shear categories

The strength of the vertical wind shear is related to the strength of the horizontal temperature gradient through the thermal wind. The strong shear classes are exceeding a vertical wind shear of $1.5 \cdot 10^{-3}\,\mathrm{s}^{-1}$ and have a median horizontal temperature gradient of around $2.0\,\mathrm{K}$ per $100\,\mathrm{km}$ (Fig. 5a). PLs within these categories thus most likely intensify through baroclinc instability. In contrast, the weak-shear category has a median temperature gradient of $1.3\,\mathrm{K}$ per $100\,\mathrm{km}$ and is thus considerably less baroclinic. While hurricane-like PLs might be feasible in this more symmetric category, there is little evidence for hurricane-like PLs within this category.

Cyclogenesis of PLs in all shear categories is further supported by a low static stability ($N \approx 0.005\,\mathrm{s}^{-1}$, Fig. 5b) relative to typical synoptic-scale baroclinic environments (see Table 2). Low static stability is associated with a higher baroclinic growth rate (Vallis, 2017). The low static stability in these PL environments implies high temperature contrast between the sea-surface and the upper troposphere associated with PLs, often expressed as SST-T_{500} (e.g. Zappa et al., 2014; Stoll et al., 2018; Bracegirdle and Gray, 2008).

The atmosphere is slightly less stable in reverse and right-shear situations (both median of $0.0048\,\mathrm{s}^{-1}$) than in forward and left-shear situations (both median of $0.0050\,\mathrm{s}^{-1}$). This was also pointed out by Terpstra et al. (2016), who found a larger temperature contrast between the sea surface and the 500 hPa level for reverse compared to forward-shear conditions. It could be argued that the shear-strength threshold of $1.5 \cdot 10^{-3}\,\mathrm{s}^{-1}$ should be lower for reverse and right-shear categories as a weaker vertical shear can be compensated by a lower static stability. We do not adapt such an adjustment, which would increase the fraction of reverse and right-shear conditions.

PL time steps with strong shear are more common in the first half of the PL lifetime (Fig. 5c) and are more often associated with a positive vorticity tendency (Fig. 5d) depicting intensification. PL time steps in the weak-shear category are predominantly occurring at later stages associated with decay (70%). Even though some PL time steps in weak shear feature intensification (30%), only 6% of these time steps are intensifying at a rate of more than $1 \cdot 10^{-5}\,\mathrm{s}^{-1}\,\mathrm{h}^{-1}$, whereas for the

https://doi.org/10.5194/wcd-2020-41
Preprint. Discussion started: 3 September 2020
© Author(s) 2020. CC BY 4.0 License.

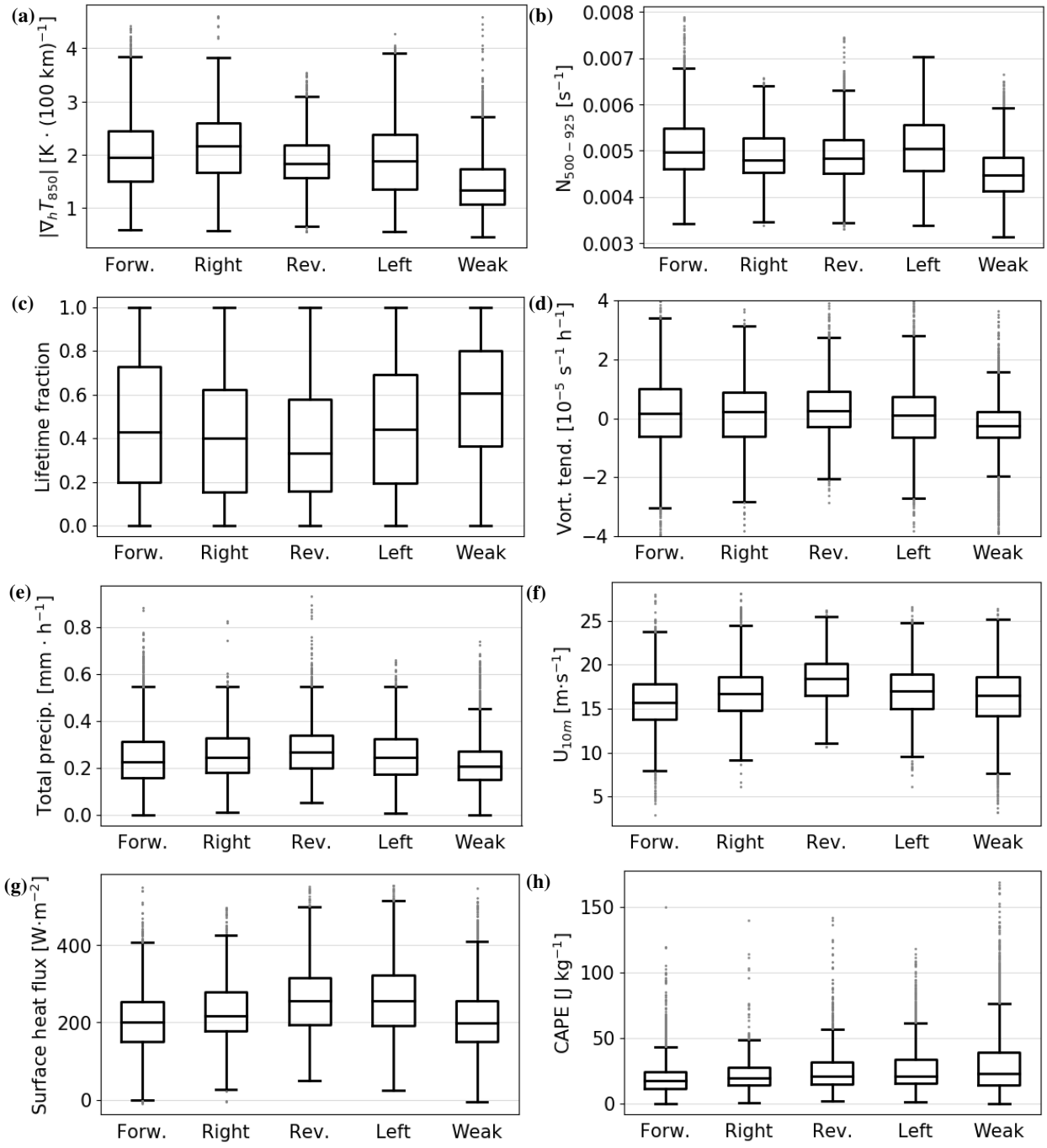

Figure 5. Distributions of different parameters for all time steps attributed to the shear categories introduced in Figure 4. The mean of the parameter within a 250 km radius is calculated, except for the 10 m wind speed, where the maximum value is used. For the computation of the mean static stability, total precipitation, surface heat fluxes, and CAPE grid cells covered by land or sea-ice are excluded.

https://doi.org/10.5194/wcd-2020-41
Preprint. Discussion started: 3 September 2020
© Author(s) 2020. CC BY 4.0 License.

high-shear categories on average 22% of the time steps are intensifying at such a rate. Closer investigation reveals that these 6% of intensifying time steps within the weak shear category feature a shear close to the threshold separating between strong and weak shear systems.

The static stability is considerably lower in the weak-shear category (median $N = 0.0044\,\mathrm{s}^{-1}$, Fig. 5b), which is most likely associated with this category appearing later during the PL life time when condensational latent-heat release has destabilised the atmosphere.

While the area-mean total precipitation is $0.24\,\mathrm{mmh}^{-1}$ (median), which is rather low compared to extra-tropical cyclones, it is somewhat stronger for reverse-shear conditions (Fig. 5e, median $0.27\,\mathrm{mmh}^{-1}$), which indicates that latent heat release by condensation is most important in this class, which may compensate for a lower baroclinicity. In weak-shear condition, there is less precipitation (median $0.21\,\mathrm{mmh}^{-1}$) than for the other categories, which is consistent with this class mainly containing the decaying stages of PLs. It further indicates that intensification solely through convective processes is highly unlikely within this class.

The area-maximum near-surface wind speed of PLs is around $16.6\,\mathrm{ms}^{-1}$ (median). The near-surface winds are somewhat lower for forward (Fig. 5f, median $\approx 15.7\,\mathrm{ms}^{-1}$) and higher for reverse-shear conditions (median $\approx 18.4\,\mathrm{ms}^{-1}$), which is consistent with Michel et al. (2018), who found that reverse-shear polar mesoscale cyclones (PMCs) have on average a stronger lifetime-maximum near-surface wind speed ($22\,\mathrm{ms}^{-1}$) than forward-shear PMCs ($19\,\mathrm{ms}^{-1}$). Hence, PL detection with a criteria on the near-surface wind speed, as suggested in the definition by Rasmussen and Turner (2003) with $15\,\mathrm{ms}^{-1}$, excludes more forward than reverse-shear systems.

In reverse-shear conditions, the environmental flow is strongest at low levels and decreases with height (node 9 in Fig. 2, 3j), which is consistent with Terpstra et al. (2016). For forward-shear conditions, the environmental-mean wind vector is weak at low levels (Fig. 3) and hence the near-surface wind is mainly associated with the cyclonic circulation of the PL (see also Fig. 2).

The area-mean turbulent heat fluxes at the surface are highest for left and reverse-shear conditions (median 257 and $256\,\mathrm{Wm}^{-2}$, respectively, Fig. 5g) and slightly lower for right, forward, and weak-shear conditions (median 216, 201 and $200\,\mathrm{Wm}^{-2}$, respectively). Higher surface turbulent heat fluxes for reverse-shear conditions were also found by Terpstra et al. (2016) and associated with the stronger near-surface winds. The higher turbulent fluxes in left-shear conditions is most likely connected to the large-scale flow being associated with cold air advection (SOM node 7 in Fig. 2). In the weak-shear category, surface fluxes are not exceptionally high, rendering it unlikely that the WISHE mechanism is active for these PLs.

All shear categories feature low values in the convective available potential energy (CAPE, Fig. 5h), with median values around $20\,\mathrm{Jkg}^{-1}$ and only few PL time steps with CAPE above $50\,\mathrm{Jkg}^{-1}$. This is in accordance with Linders and Saetra (2010), who found that CAPE is consumed instantaneously during PL development as it is produced. In order to be of dynamic relevance, CAPE values would need to be at least one order of significantly larger (Markowski and Richardson, 2011). Hence the CISK mechanism that relies on CAPE appears unlikely to explain intensification of PLs in the STARS dataset.

https://doi.org/10.5194/wcd-2020-41
Preprint. Discussion started: 3 September 2020
© Author(s) 2020. CC BY 4.0 License.

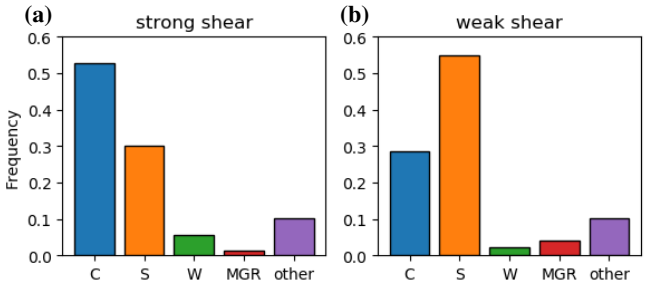

Figure 6. Occurrence of the cloud morphologies introduced by Rojo et al. (2019) within for the time steps with a strong (left) and weak (right) vertical shear. The cloud morphologies are: C = comma shaped, S = spirali form, W = wave system, MGR = merry-go-round.

3.4 Cloud morphology

Strong-shear conditions most commonly feature comma-shaped clouds (53% of the labelled time steps by Rojo et al. (2019)), whereas spirali-form clouds are less frequent in these categories (30%, Fig. 6). Weak-shear conditions, on the other hand, feature mainly spirali-form clouds (55%) and less frequently comma clouds (29%). This is consistent with the findings of Yanase and Niino (2007) that the cloud structure is connected to the baroclincity of the environment.

However, we find little evidence for axis-symmetric intensification in an environment with weak shear. Accordingly, the axis-symmetric, spirali-form system simulated by Yanase and Niino (2007) had a considerably lower growth rate than the systems within a baroclinic environment (their Fig. 3). Instead, time steps in the weak-shear category resemble the occlusion stage of a baroclinic development (Fig. 2) with a quasi-barotropic alignment of the flow (Fig. 3). The spirali-form cloud signature may be explained by a baroclinic development with a warm seclusion, as suggested by the Shapiro-Keyser model (Shapiro and Keyser, 1990). In later stages, this model resembles a spirali-form cloud signature. We therefore propose the warm seclusion pathway as an alternative hypothesis for the formation of hurricane-like PLs.

The frequency of wave-type clouds (Rojo et al., 2015) is higher within the strong shear (6%) than the weak-shear category (2%). Similar to comma-clouds, wave-type clouds are often associated with a baroclinic development (Rasmussen and Turner, 2003). The frequency of merry-go-round systems is higher within the weak shear (4%) compared to the strong-shear categories (1%). Merry-go-round are often associated with an upper-level cold cut-off low in the absence of considerable baroclinicity (Rasmussen and Turner, 2003).

3.5 Synoptic conditions associated with the shear categories

Within the Nordic Seas, each of the shear categories is associated with a distinct synoptic-scale situation (Fig. 7). PLs in forward-shear conditions typically form when a synoptic-scale low pressure system is located in the north-eastern Barents Sea causing a marine cold-air outbreak around Svalbard (Fig. 7a). Most PLs within this category occur south of Svalbard and feature an eastward propagation.

https://doi.org/10.5194/wcd-2020-41
Preprint. Discussion started: 3 September 2020
© Author(s) 2020. CC BY 4.0 License.

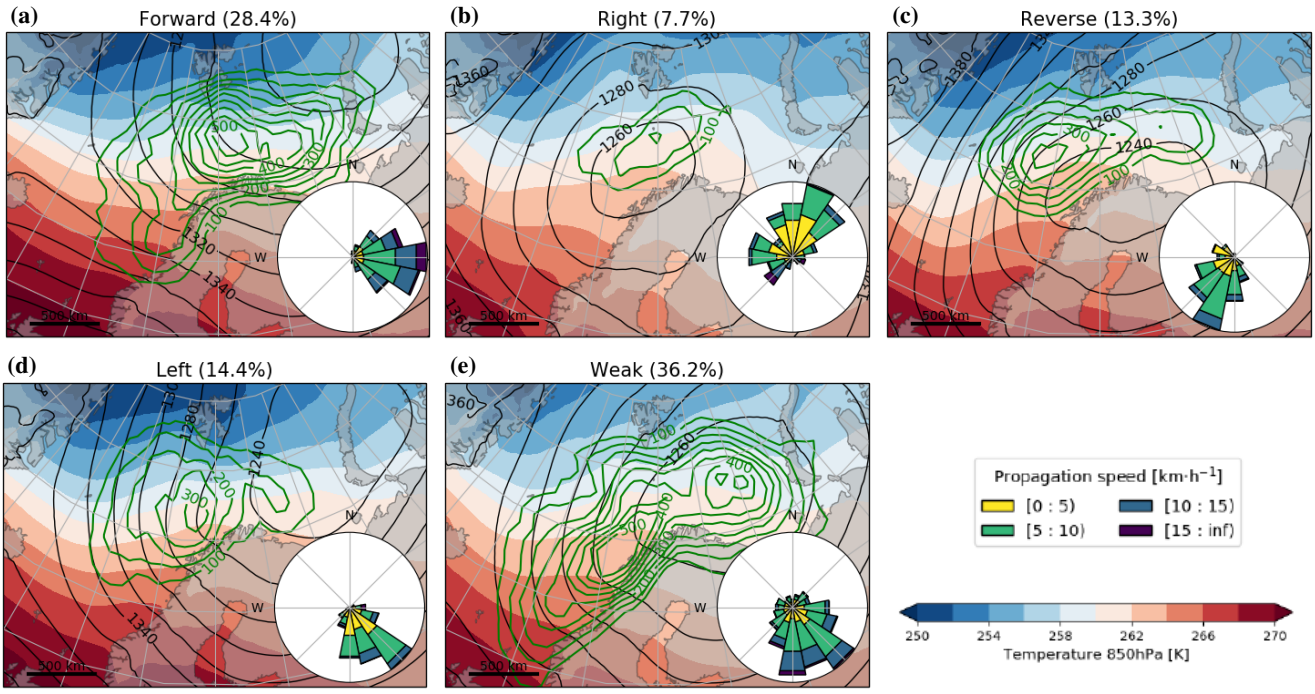

Figure 7. Composite maps of the 850 hPa temperature (shading) and geopotential height (black contours) associated with the polar lows within each shear category. Green contours: Track densities associated with each category calculated by the number of track points within a 250 km radius. The roses depict the track distribution of the propagation direction and speed.

The synoptic-scale situation for reverse-shear PLs mainly features a low-pressure system over northern Scandinavia leading to a cold-air outbreak to the west of Svalbard (Fig. 7c). In the Norwegian Sea, where most reverse-shear PLs develop, the flow is south-westward, consistent with the direction of propagation of these PLs. The typical location and propagation directions of forward and reverse-shear PL is in accordance with (Terpstra et al., 2016; Michel et al., 2018).

In left-shear conditions, a low pressure system is located over the Barents Sea causing a south- to south-eastward flow towards a warmer environment (Fig. 7c). PLs primarily occur to the south of Svalbard at the leading edge of the cold-air outbreak. Right-shear PLs predominantly occur to the east and north-east of a synoptic-scale low located in the Norwegian Sea (Fig. 7d). In this situation, PLs propagate north- and westward into colder air masses.

Weak-shear conditions are more variable than the other categories (Fig. 7e). PLs occur most frequently in more southerly locations near the coast of Norway and in the eastern Barents Sea, corresponding to lysis locations. A separation of the weak-shear conditions for different areas (not shown) reveals that they primarily occur downstream of one of the strong-shear categories within an area of low temperature contrast. The latter is consistent with this category mainly being associated with mature and decaying PLs that originated from one of the other categories.

https://doi.org/10.5194/wcd-2020-41
Preprint. Discussion started: 3 September 2020
© Author(s) 2020. CC BY 4.0 License.

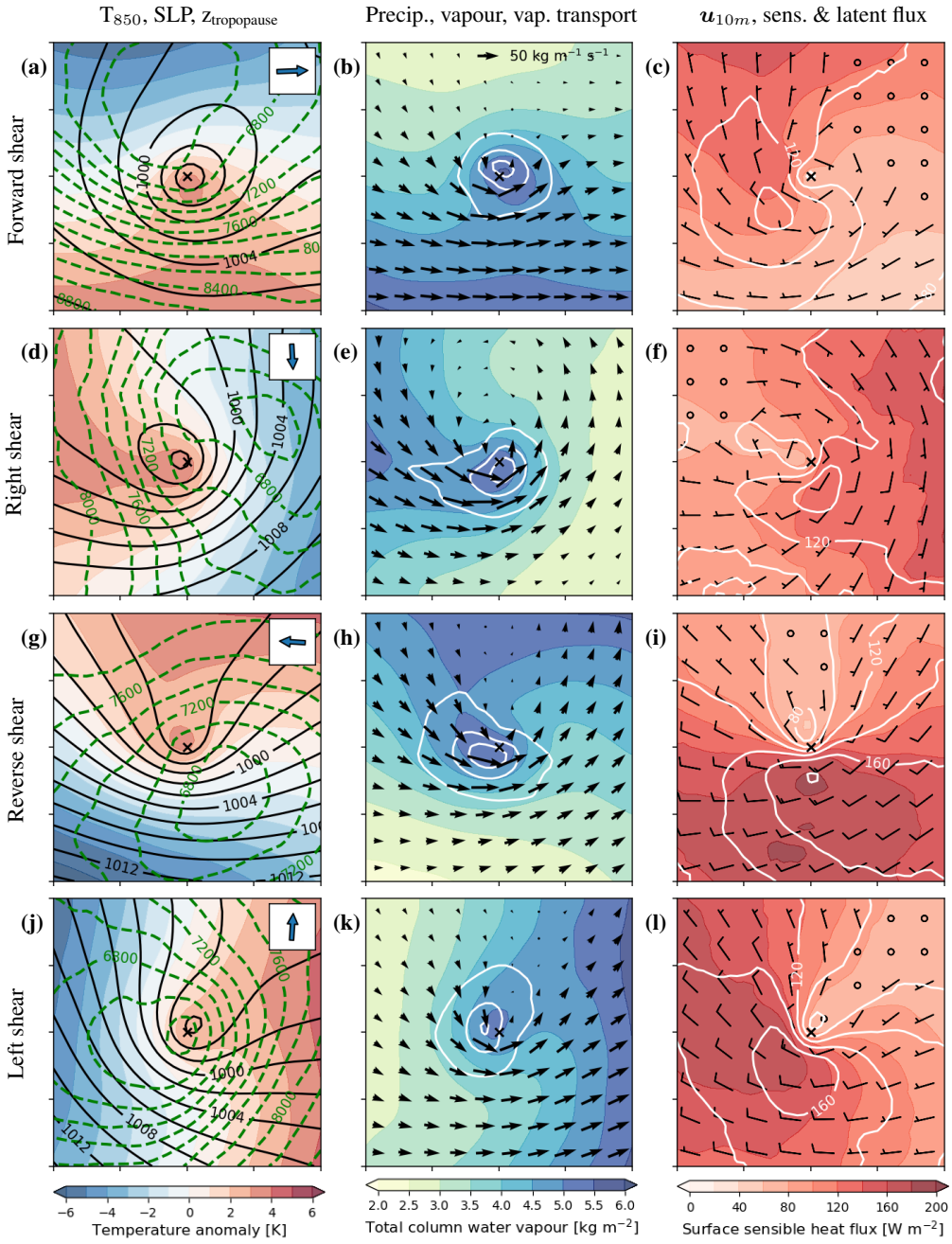

Figure 8. Composite maps in a PL-centred grid with propagation direction towards the right associated with four strong-shear categories. Left column: temperature anomaly at 850 hPa (shading), sea-level pressure (black contours, 2 hPa spacing), and tropopause height (green-dashed contours, spacing 200 m). The inset shows the mean of the vertical-shear vector within the category (compare to Fig. 4). Middle column: Total column water vapour (shading), total precipitation (contours, 0.2 $\mathrm{mmh^{-1}}$ spacing), and vertically integrated water vapour flux (arrow, reference vector at top). Right column: 10 m wind vectors (quivers), surface sensible heat flux (shading) and surface latent heat flux (contours, spacing 20 $\mathrm{Wm^{-2}}$).

https://doi.org/10.5194/wcd-2020-41
Preprint. Discussion started: 3 September 2020
© Author(s) 2020. CC BY 4.0 License.

4 Intensification mechanisms

4.1 Baroclinic setup

The temperature as well as the upper and lower-level flow field for forward-shear PLs (Fig. 8a) resembles the structure of a smaller version of a mid-latitude baroclinic cyclone that develops along the polar front featuring a typical up-shear tilt with height of the low-pressure anomaly (e.g. Dacre et al., 2012), where the trough axis of the tropopause depression is displaced against the shear vector compared to the closed surface-pressure circulation. Reverse-shear systems, are characterised by an intense low-level trough together with a tropopause trough that is centred up-shear (Fig. 8g).

Right and left-shear conditions are characterised by a closed low-level vortex or a low-level trough, respectively, and feature a tropopause depression with its trough axis located up-shear (Fig. 8d,j). Thus, all strong-shear categories feature an up-shear vertical tilt between the surface pressure anomaly and the upper-level depression, which is characteristic for baroclinic development (Holton, 1973).

Consistent with the vertical tilt of the pressure anomaly, the low-level circulation is associated with down-gradient warm-air advection down-shear in the warm sector. For forward (reverse) shear conditions, the warm sector is ahead of (behind) the PL with respect to its propagation. For right (left) conditions, the warm sector lies to the right (left) side of the PL track. Analogously, the low-level circulation is associated with an up-gradient cold-air advection in the cold sector, which is located up-shear. Low-level temperature advection by the cyclone generates eddy available potential energy and contributes to the amplification of the PL (see first term of equation 5 in Terpstra et al. (2015)).

The upper-level trough is associated with ascent at its leading edge (Supplementary Figure 11) located near the surface pressure anomaly and hence leads to a further intensification of the PL through vorticity stretching. The ascending air is co-located to the precipitation (second column in Fig. 8). The ascent occurs in an area that is close to conditional instability ($\theta_{e,2m} - \theta_{e,500hPa} \approx -6\,K$, Supplementary Figure 11).

The interaction between the upper and lower levels is further supported by a low vertical stability up to the tropopause at around 400 hPa (Fig. 5d). This suggests that the baroclinic development spans the entire depth of the troposphere and is not confined to the low levels as suggested by Mansfield (1974).

4.2 Diabatic contribution

Most of the precipitation occurs along the warm front in the sector left down-shear of the PL centre (Fig. 8), which is also the location of the increased cloud cover featuring a comma-shaped form (Fig. 2). The release of latent heat associated with the precipitation leads to the production of potential vorticity underneath the level of strongest heating and hence intensifies the low-level circulation. As the latent heat release primarily occurs in the warm sector, it further increases the horizontal temperature gradient, which contributes to the generation of eddy available potential energy (Terpstra et al., 2015).

For all shear conditions, the moisture that is converted to precipitation originates from the warm sector. In forward and left-shear conditions, PLs are propagating towards the warm and moist sector (Fig. 8b,k), while the moisture is transported into the area of precipitation from the rear of the PL in reverse and right-shear conditions.

https://doi.org/10.5194/wcd-2020-41
Preprint. Discussion started: 3 September 2020
© Author(s) 2020. CC BY 4.0 License.

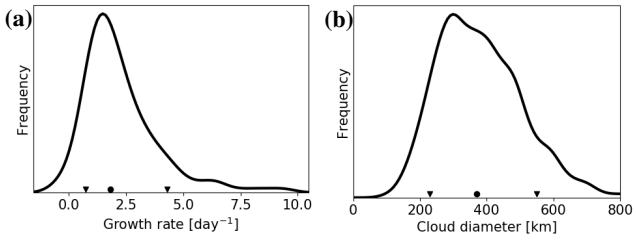

Figure 9. (a) Distribution of the lifetime-maximum in the growth rate of the PL. (b, c) Distribution of the diameter for all PL time steps based on the cloud diameter according to Rojo et al. (2019). The dot denotes the median, and the triangles the 10th and 90th percentiles of the distributions. The curves are computed with a Gaussian kernel.

Table 2. Approximation of values required for the determination of the growth rate, σ_{max}, and the diameter, d_σ, of the fastest growing mode by dry-baroclinic theory. For PLs, the static stability, N, is obtained from Figure 5, the shear strength, $\frac{\partial u_s}{\partial z}$, from Figure 4, the tropopause level, H, from Figure 8. The Coriolis parameter, f, is computed for 70°and 45°latitude for PLs and mid-latitude cyclones, respectively. For mid-latitude cyclones N, $\frac{\partial u_s}{\partial z}$ and H are approximated with the use of values from Figure 2b, 3h and 3i, respectively, of Stoll et al. (2018).

	N [s^{-1}]	$\frac{\partial u_s}{\partial z}$ [s^{-1}]	H [m]	f [s^{-1}]	σ_{max} [day^{-1}]	d_σ [km]
Polar lows	0.005	$2 \cdot 10^{-3}$	7,000	$1.4 \cdot 10^{-4}$	1.5	500
Mid-latitude cyclones	0.012	$3 \cdot 10^{-3}$	9,000	$1.0 \cdot 10^{-4}$	0.6	2,400

The highest sensible heat fluxes occur on the cold side of the PL (Fig. 8c,f,i,l), leading to a reduction of low-level baroclinicity and a diabatic loss of eddy available potential energy. Latent heat fluxes are roughly co-located with the sensible heat fluxes, but occur further downstream where the air mass is already warmer and has therefore a higher capacity for water vapour. As the highest latent heat fluxes occur in the cold sector, the moisture released there would need to be advected around the PL to contribute to the diabatic intensification in the warm sector. Therefore, the latent heat flux appears to have a limited direct effect on the intensification of the PL. However, the latent heat fluxes in the warm sector yield an additional source of moisture that can more directly contribute to intensify the precipitation.

The distribution of the heat fluxes does, however, not contradict that the fluxes are important in creating an environment conducive for PL development. Sensible heat fluxes prior and during the PL development create an environment of low static stability, which supports the baroclinic intensification. Even though the highest latent heat fluxes are displaced from the warm sector, the polar air mass in which the PL develops benefits from the surface evaporation that fuels the diabatic contribution from latent heat release.

https://doi.org/10.5194/wcd-2020-41
Preprint. Discussion started: 3 September 2020
© Author(s) 2020. CC BY 4.0 License.

4.3 Scale considerations

Given the dry-baroclinic growth rate $\sigma_{max} = 0.3\frac{f}{N}\frac{\partial \boldsymbol{u_s}}{\partial z}$ and diameter of the most unstable mode $d_\sigma \approx 2\frac{NH}{f}$ (e.g. p.354ff Vallis, 2017), inserting typical values for PLs results in $\sigma_{max} \approx 1.5\,\mathrm{day}^{-1}$ and $d_\sigma \approx 500\,\mathrm{km}$ (Table 2), where the growth rate is close to observed PLs ($\approx$1.8 day^{-1}, Fig.9a).

These values are quite different to typical mid-latitude cyclones, with $\sigma_{max} \approx 0.6\,\mathrm{day}^{-1}$ and $d_\sigma \approx 2400\,\mathrm{km}$ (Table 2), where the largest contribution to the faster growth and smaller scale of PLs appears to be due to the reduced static stability for PLs ($N \approx 0.005\,\mathrm{s}^{-1}$) compared to mid-latitude cyclones ($N \approx 0.012\,\mathrm{s}^{-1}$). The larger Coriolis parameter, f, and lower tropospheric depth, H, contribute only to a smaller extent and the vertical-shear, $\frac{\partial \boldsymbol{u_s}}{\partial z}$ is actually weaker for PLs compared to mid-latitude cyclones.

The estimation of the size of PLs is challenging. Often the diameter of the cloud associated with the PL is utilised for this purpose (e.g. Rojo et al., 2015), where the typical cloud diameter based on Rojo et al. (2019) is around 370 km (median, Fig. 9b). The cloud size estimated for the medium-level comma-shaped clouds of SOM 1, 3, 7 and 9 in Figure 2 is around 400 km. The vertical tilt between the upper and lower-level pressure disturbance (Fig. 8a,d,g), which in dry-baroclinic theory is a quarter of the wavelength of the fastest growing mode, is approximately 200 km, confirming the estimated diameter of around 400 km. Hence, the observed diameters are close to the theoretical estimates.

The slight discrepancies between observation and theory are most likely attributable to latent heat release, which is observed for all shear configurations (Fig. 8b,e,h,k). The release of latent heat increases the growth rate and reduces the diameter of the fastest growing mode (Sardie and Warner, 1983; Yanase and Niino, 2007; Terpstra et al., 2015). Moist-baroclinic instability therefore appears to be the most plausible intensification mechanism for PLs, which was also proposed by Terpstra et al. (2015) and Haualand and Spengler (2020).

5 Discussion and conclusion

We applied the SOM algorithm to the 850 hPa temperature anomaly field to identify archetypal meteorological configurations of PL environments (Fig. 2). The application of the algorithm to other atmospheric fields, such as the temperature anomaly at different height levels, specific humidity, and upper or lower-level geopotential height anomaly reveal similar results, which demonstrates the generality of our results.

The different nodes in the SOM matrix can be categorised by the vertical-shear vector with respect to the propagation direction (Fig. 4). We used a threshold of $1.5 \cdot 10^{-4}\,\mathrm{s}^{-1}$ to classify the vertical-shear vector into strong directional shear categories above this threshold and weak-shear conditions below. Our analysis confirms the usefulness of the classification suggested by Duncan (1978) into forward and reverse-shear PLs with the vertical-shear vector in the same or opposite direction of the PL propagation, respectively. In addition to the previously identified shear categories, we find PL configurations that feature a shear vector directed to the left or right with respect to the propagation of the PLs, which we refer to as left or right-shear conditions, respectively.

https://doi.org/10.5194/wcd-2020-41
Preprint. Discussion started: 3 September 2020
© Author(s) 2020. CC BY 4.0 License.

Forward-shear PLs occur predominantly in an eastward flow in the Barents Sea with cold air to the left of the direction of propagation (Fig. 7a). Reverse-shear PLs mainly develop in the Norwegian Sea in a southward flow with cold air on the right-hand side. Left-shear PLs occur at the leading edge of cold air outbreaks and propagate towards a warmer environment, while right-shear PLs propagate towards a colder environment and occur when warmer air is advected towards a polar air mass. The shear situation of an individual PL can, however, change during its lifetime.

The baroclinic structure of the four strong shear categories features a vertical tilt between the surface and upper-level pressure anomaly against the vertical-shear vector (Fig. 8). The upper-level anomaly is captured by a tropopause depression, indicating that PL span the entire depth of the polar troposphere. The atmospheric configuration features the classic growth through baroclinic instability, where the anomalies are organised by the vertical-shear vector. Therefore, the classification of PLs based on their environmental thermal fields successfully reveals the dominant development mechanism.

Weak-shear conditions are predominantly associated with spirali-form clouds, whereas strong-shear situations with comma-shaped clouds (Fig. 6). However, weak-shear situations occur mainly at the end of the PL lifetime and are seldomly associated with a considerable intensification. Consistent with the cloud structure, precipitation mainly develops along the warm front in the sector between the direction of the vertical-shear vector and its left side.

The surface latent heat fluxes appear to be only indirectly relevant, as the maxima in the latent heat flux are significantly displaced from the precipitation. Instead, most moisture converges from the warm and moist side of the PL, as was previously observed by Terpstra et al. (2015); Stoll et al. (2020). The direct effect of surface sensible heat fluxes would act to reduce the environmental temperature gradient and thereby most likely contributes to a dampening of the development. However, surface fluxes also shape the environment in which the PLs develop, where polar air masses would be relatively dry without experiencing significant latent heat fluxes. The sensible heat flux reduces the static stability, which is also conducive for baroclinic development.

Applying dry-baroclinic theory to atmospheric values for PL environments yields growth rates and diameters that are comparable to observed PLs, where the discrepancies can most likely be attributed to latent heat release, which enhances growth and reduces the scale (e.g., Sardie and Warner, 1983; Terpstra et al., 2015; Haualand and Spengler, 2020). We therefore suggest that moist-baroclinc development is the dominant mechanism leading to the intensification of the majority of PLs. The considerably higher growth rates and smaller disturbance scale of PLs as compared to mid-latitude cyclones appear to be primarily associated with a lower static stability and to a lesser extent to a higher Coriolis parameter and a lower tropopause height. The lower stability is associated with the moist-adiabatic lapse rate in cold air outbreaks (Linders and Saetra, 2010), which, due to the low temperatures of polar air masses, is nearly equivalent to the dry adiabat.

Generally our analysis provides no evidence for the existence of hurricane-like PLs that intensifies mainly by latent heat release. This casts doubt on the PL spectrum ranging from comma-shaped, baroclinic systems to spirali-form, hurricane-like types. Instead, most PLs intensify in a baroclinic environment characterised by a strong vertical shear. However, PLs often develop a warm core (e.g. Bond and Shapiro, 1991; Nordeng and Rasmussen, 1992; Føre et al., 2011), which is typical for baroclinic development following the Shapiro-Keyser model with a warm seclusion and a spirali-form cloud structure at the later stages of the life cycle (Shapiro and Keyser, 1990). Hence, PLs with spirali-form clouds are most likely best described

https://doi.org/10.5194/wcd-2020-41
Preprint. Discussion started: 3 September 2020
© Author(s) 2020. CC BY 4.0 License.

as secluded cyclones, as was argued for previously (Hewson et al., 2000). To further clarify this hypothesis, studies using high-resolution datasets, such as CARA (CAR), should be used to investigate the frontal lifecycle in PLs.

Data availability. The tracks of the ERA-5 matched STARS PLs are provided.

Author contributions. PS designed the study and performed the analysis. All authors contributed to the discussion of the methods and results. PS wrote the manuscript with contributions from all authors.

Competing interests. The authors declare no competing interests.

Acknowledgements. We thank ECMWF for providing access to data from the ERA-5 reanalysis. Parts of the data were processed at the supercomputer Stallo provided by the Norwegian Metacenter for Computational Science (NOTUR) under the project NN9348K. We also thank Denis Sergeev for providing access and support to the PMC-tracking algorithm and Tiina Nygård for sharing code for the application of the SOM algorithm.

https://doi.org/10.5194/wcd-2020-41
Preprint. Discussion started: 3 September 2020
© Author(s) 2020. CC BY 4.0 License.

References

Copernicus Arctic Regional Reanalysis Service, https://climate.copernicus.eu/copernicus-arctic-regional-reanalysis-service, accessed: 2020-06-11.

Bond, N. A. and Shapiro, M.: Polar lows over the Gulf of Alaska in conditions of reverse shear, Monthly weather review, 119, 551–572, 1991.

Bracegirdle, T. J. and Gray, S. L.: An objective climatology of the dynamical forcing of polar lows in the Nordic seas, International Journal of Climatology, 28, 1903–1919, 2008.

Businger, S. and Reed, R. J.: Cyclogenesis in cold air masses, Weather and Forecasting, 4, 133–156, 1989.

Charney, J. G. and Eliassen, A.: On the growth of the hurricane depression, Journal of the Atmospheric Sciences, 21, 68–75, 1964.

Claud, C., Heinemann, G., Raustein, E., and McMurdie, L.: Polar low le Cygne: satellite observations and numerical simulations, Quarterly Journal of the Royal Meteorological Society, 130, 1075–1102, 2004.

Dacre, H., Hawcroft, M., Stringer, M., and Hodges, K.: An extratropical cyclone atlas: A tool for illustrating cyclone structure and evolution characteristics, Bulletin of the American Meteorological Society, 93, 1497–1502, 2012.

De Boor, C., De Boor, C., Mathématicien, E.-U., De Boor, C., and De Boor, C.: A practical guide to splines, vol. 27, springer-verlag New York, 1978.

Duncan, C.: Baroclinic instability in a reversed shear-flow, Meteorological Magazine, 107, 17, 1978.

Emanuel, K. A.: An air-sea interaction theory for tropical cyclones. Part I: Steady-state maintenance, Journal of the Atmospheric Sciences, 43, 585–605, 1986.

Emanuel, K. A. and Rotunno, R.: Polar lows as arctic hurricanes, Tellus A, 41, 1–17, 1989.

Forbes, G. S. and Lottes, W. D.: Classification of mesoscale vortices in polar airstreams and the influence of the large-scale environment on their evolutions, Tellus A: Dynamic Meteorology and Oceanography, 37, 132–155, 1985.

Føre, I., Kristjánsson, J. E., Saetra, Ø., Breivik, Ø., Røsting, B., and Shapiro, M.: The full life cycle of a polar low over the Norwegian Sea observed by three research aircraft flights, Quarterly Journal of the Royal Meteorological Society, 137, 1659–1673, 2011.

Føre, I., Kristjánsson, J. E., Kolstad, E. W., Bracegirdle, T. J., Saetra, Ø., and Røsting, B.: A 'hurricane-like'polar low fuelled by sensible heat flux: high-resolution numerical simulations, Quarterly Journal of the Royal Meteorological Society, 138, 1308–1324, 2012.

Harrold, T. and Browning, K.: The polar low as a baroclinic disturbance, Quarterly Journal of the Royal Meteorological Society, 95, 710–723, 1969.

Haualand, K. F. and Spengler, T.: Direct and Indirect Effects of Surface Fluxes on Moist Baroclinic Development in an Idealized Framework, Journal of the Atmospheric Sciences, pp. 1–43, 2020.

Hersbach, H. and Dee, D.: ERA5 reanalysis is in production, ECMWF newsletter, 147, 5–6, 2016.

Hewson, T., Craig, G., and Claud, C.: Evolution and mesoscale structure of a polar low outbreak, Quarterly Journal of the Royal Meteorological Society, 126, 1031–1063, 2000.

Holton, J. R.: An introduction to dynamic meteorology, American Journal of Physics, 41, 752–754, 1973.

Jonassen, M. O., Chechin, D., Karpechko, A., Lüpkes, C., Spengler, T., Tepstra, A., Vihma, T., and Zhang, X.: Dynamical processes in the Arctic atmosphere, in: Physics and Chemistry of the Arctic Atmosphere, pp. 1–51, Springer, 2020.

Kohonen, T., Schroeder, M., Huang, T., and Maps, S.-O.: Springer-Verlag New York, Inc., Secaucus, NJ, 43, 2001.

https://doi.org/10.5194/wcd-2020-41
Preprint. Discussion started: 3 September 2020
© Author(s) 2020. CC BY 4.0 License.

Kolstad, E. W. and Bracegirdle, T.: Sensitivity of an apparently hurricane-like polar low to sea-surface temperature, Quarterly Journal of the Royal Meteorological Society, 143, 966–973, 2017.

Kolstad, E. W., Bracegirdle, T. J., and Zahn, M.: Re-examining the roles of surface heat flux and latent heat release in a "hurricane-like" polar low over the Barents Sea, Journal of Geophysical Research: Atmospheres, 121, 7853–7867, 2016.

Kristjánsson, J. E., Barstad, I., Aspelien, T., Føre, I., Godøy, Ø., Hov, Ø., Irvine, E., Iversen, T., Kolstad, E., Nordeng, T., et al.: The Norwegian IPY–THORPEX: Polar lows and Arctic fronts during the 2008 Andøya campaign, Bulletin of the American Meteorological Society, 92, 1443–1466, 2011.

Laffineur, T., Claud, C., Chaboureau, J.-P., and Noer, G.: Polar lows over the Nordic Seas: Improved representation in ERA-Interim compared to ERA-40 and the impact on downscaled simulations, Monthly Weather Review, 142, 2271–2289, 2014.

Linders, T. and Saetra, Ø.: Can CAPE maintain polar lows?, Journal of the atmospheric sciences, 67, 2559–2571, 2010.

Mansfield, D.: Polar lows: The development of baroclinic disturbances in cold air outbreaks, Quarterly Journal of the Royal Meteorological Society, 100, 541–554, 1974.

Markowski, P. and Richardson, Y.: Mesoscale meteorology in midlatitudes, vol. 2, John Wiley & Sons, 2011.

Michel, C., Terpstra, A., and Spengler, T.: Polar Mesoscale Cyclone Climatology for the Nordic Seas Based on ERA-Interim, Journal of Climate, 31, 2511–2532, 2018.

Noer, G. and Lien, T.: Dates and Positions of Polar lows over the Nordic Seas between 2000 and 2010, Met. no report, 16, 2010, 2010.

Nordeng, T. E. and Rasmussen, E. A.: A most beautiful polar low. A case study of a polar low development in the Bear Island region, Tellus A, 44, 1992.

Nygård, T., Graversen, R. G., Uotila, P., Naakka, T., and Vihma, T.: Strong dependence of wintertime Arctic moisture and cloud distributions on atmospheric large-scale circulation, Journal of Climate, 32, 8771–8790, 2019.

Ooyama, K.: A dynamical model for the study of tropical cyclone development, Geofisica Internacional (Mexico), 4, 187–198, 1964.

Rasmussen, E.: The polar low as an extratropical CISK disturbance, Quarterly Journal of the Royal Meteorological Society, 105, 531–549, 1979.

Rasmussen, E. A. and Turner, J.: Polar lows: Mesoscale Weather Systems in the Polar Regions, Cambridge University Press: Cambridge, UK, 2003.

Reed, R. J.: Cyclogenesis in polar air streams, Monthly Weather Review, 107, 38–52, 1979.

Reed, R. J. and Blier, W.: A Case Study of Comma Cloud Development in the Eastern Pacific, Monthly Weather Review, 114, 1681–1695, 1986.

Reed, R. J. and Duncan, C. N.: Baroclinic instability as a mechanism for the serial development of polar lows: a case study, Tellus A, 39, 376–384, 1987.

Renfrew, I.: SYNOPTIC METEOROLOGY | Polar Lows, in: Encyclopedia of Atmospheric Sciences (Second Edition), edited by North, G. R., Pyle, J., and Zhang, F., pp. 379 – 385, Academic Press, Oxford, 2015.

Rojo, M., Claud, C., Mallet, P.-E., Noer, G., Carleton, A. M., and Vicomte, M.: Polar low tracks over the Nordic Seas: a 14-winter climatic analysis, Tellus A, 67, 2015.

Rojo, M., Noer, G., and Claud, C.: Polar Low tracks in the Norwegian Sea and the Barents Sea from 1999 until 2019, https://doi.org/10.1594/PANGAEA.903058, supplement to: Rojo et al. (2019), 2019.

Sardie, J. M. and Warner, T. T.: On the Mechanism for the, Development of Polar Lows, Journal of the Atmospheric Sciences, 40, 869–881, 1983.

https://doi.org/10.5194/wcd-2020-41
Preprint. Discussion started: 3 September 2020
© Author(s) 2020. CC BY 4.0 License.

Savitzky, A. and Golay, M. J.: Smoothing and differentiation of data by simplified least squares procedures., Analytical chemistry, 36, 1627–1639, 1964.

Shapiro, M. A. and Keyser, D.: Fronts, jet streams and the tropopause, in: Extratropical cyclones, pp. 167–191, Springer, 1990.

Smirnova, J. E. and Golubkin, P. A.: Comparing polar lows in atmospheric reanalyses: Arctic System Reanalysis versus ERA-Interim, Monthly Weather Review, 2017.

Stoll, P. J., Graversen, R. G., Noer, G., and Hodges, K.: An objective global climatology of polar lows based on reanalysis data, Quarterly Journal of the Royal Meteorological Society, 2018.

Stoll, P. J., Valkonen, T. M., Graversen, R. G., and Noer, G.: A well-observed polar low analysed with a regional and a global weather-prediction model, Quarterly Journal of the Royal Meteorological Society, 146, 1740–1767, https://doi.org/10.1002/qj.3764, 2020.

Terpstra, A., Spengler, T., and Moore, R. W.: Idealised simulations of polar low development in an Arctic moist-baroclinic environment, Quarterly Journal of the Royal Meteorological Society, 141, 1987–1996, 2015.

Terpstra, A., Michel, C., and Spengler, T.: Forward and reverse shear environments during polar low genesis over the North East Atlantic, Monthly Weather Review, 144, 1341–1354, 2016.

Vallis, G. K.: Atmospheric and oceanic fluid dynamics, Cambridge University Press, 2017.

Watanabe, S.-i. I., Niino, H., and Yanase, W.: Climatology of polar mesocyclones over the Sea of Japan using a new objective tracking method, Monthly Weather Review, 144, 2503–2515, 2016.

Wehrens, R., Buydens, L. M., et al.: Self-and super-organizing maps in R: the Kohonen package, Journal of Statistical Software, 21, 1–19, 2007.

Yanase, W. and Niino, H.: Dependence of polar low development on baroclinicity and physical processes: An idealized high-resolution numerical experiment, Journal of the Atmospheric Sciences, 64, 3044–3067, 2007.

Yanase, W., Fu, G., Niino, H., and Kato, T.: A polar low over the Japan Sea on 21 January 1997. Part II: A numerical study, Monthly Weather Review, 132, 1552–1574, 2004.

Zappa, G., Shaffrey, L., and Hodges, K.: Can polar lows be objectively identified and tracked in the ECMWF operational analysis and the ERA-Interim reanalysis?, Monthly Weather Review, 142, 2596–2608, 2014.